Appendix A: The Measured Intensity

In the following the formula that describes the measured intensity distribution of a diffraction feature obtained by a longitudinal scan in specular geometry is derived. The discussion will mainly focus on the longitudinal Laue pattern observed from the thin EuTe samples but can be applied to any longitudinally measured magnetic intensity distribution with only slight modifications that depend on the magnetic structure. The derivation is based on the commonly used scattering picture in the kinematical theory of x-ray diffraction. The most important aspects to discuss with respect to the analysis within this thesis are the following questions: How do the layer-dependent magnetizations enter the theoretically derived formula of the entire structure factor. That is by no means obvious, since resonant magnetic scattering from an atom is influenced by the unit vector of the local magnetization at each atomic place. Secondly, how is the theoretical formula, which quantifies the differential scattering cross section as a function of momentum transfer connected to the measured property. This question includes the proper consideration of the detector acceptance as well as several geometry dependences. In general, the property measured is the number of photons scattered into a certain fraction of the solid angle given by the detector position (2Θ) and its acceptance. The number of scattered photons can be expressed as the integral over the differential scattering cross section $\frac{d\sigma}{d\Omega}(\mathbf{Q})$:

$$I_{meas}(2\Theta) \propto \Phi_0 \int_{detector} \frac{d\sigma}{d\Omega}(\mathbf{Q}) d\Omega \quad , \tag{7.17}$$

with Φ_0 the incident photon flux (photons per second and unit area). The differential cross section, which refers to the entire macroscopic sample, quantifies the amount of photons, scattered into an infinitesimal small fraction of the solid angle as a function of the scattering vector $\mathbf{Q}$, which is quantified by the corresponding incidence and detection angles according to the equations given in chapter 3.6. The differential scattering cross section is given by the absolute square of the lattice sum $S(\mathbf{Q})$. In the present case, the magnetic scattering occurs exclusively at the Eu ions. The Te ions do not contribute to the measured magnetic intensity. Therefore, the only structure involved is the fcc Eu^{2+} sublattice with the (111) planes parallel to the surface. According to the kinematical theory the squared lattice sum reads:

$$|S(\mathbf{Q})|^2 \propto \left| \sum_{\mathbf{r_a}} f_{mag}(\epsilon^{'} \times \epsilon) \mathbf{m_a} e^{i\mathbf{Q}\mathbf{r_a}} \right|^2 \quad , \tag{7.18}$$

where f_{mag} denotes the resonant atomic magnetic form factor and $(\epsilon^{'} \times \epsilon)\mathbf{m_a}$ the polarization dependence of the circular dichroic magnetic scattering contribution which causes the observed magnetic signals. $\mathbf{m_a}$ is the unit vector pointing along the local direction of the magnetic moment of the atom at the position $\mathbf{r_a}$. Absorption is included by taking $\mathbf{Q}$ as a complex quantity. In principle, the lateral phase shift of adjacent (111) planes should be taken into account. However, in the specular geometry, the in-plane component of the scattering vector $\mathbf{Q}_{||}$ is almost zero. We therefore neglect the small lateral offset of the different (111) planes and treat them as identical. In the case of a limited number

N_z of contributing (111) planes of distance c, we can rewrite Eq. 7.18 in the form:

$$|S(\mathbf{Q})|^2 \propto |f_{mag}|^2 \left| \sum_{j=0}^{N_z-1} e^{iQ_z jc} \left(\sum_k (\epsilon^{'} \times \epsilon) \mathbf{m_{j,k}}\, e^{i\mathbf{Q}_{||}\mathbf{r}_{||}(k)} \right) \right|^2 \quad . \tag{7.19}$$

Note, that all $\mathbf{m(j,k)}$ are unit vectors. The influence of the thermal disturbance only manifests itself in the temporal average. We now introduce the order parameter: Each layer shall be characterized by a macroscopic magnetization direction specified by the unit vector along that direction $\mathbf{m_0}(j)$, which, in the case of the simple AFM structure of EuTe, is given by $\mathbf{m_0}(j) = (-1)^j \mathbf{m_0}$. The decreasing order with temperature is described by a homogeneous decrease of the average local moment along that direction: At each time the local direction of a spin has a component m_o along $\mathbf{m_0}$ and a perpendicular component m_d with $m_o^2 + m_d^2 = 1$, characterized by a temporal average in the ordered phase of $< m_o >= m > 0$ and $< m_d >= 0$ where m denotes the local order parameter, which should be equal for all spins within the same layer. Thus, the layer-dependent order parameter $m(j)$ is defined as the average spin direction along the magnetization direction $\mathbf{m_0}(j)$. The deviations of the local spin directions from $\mathbf{m_0}$ at different lattice sites will give rise to a weak scattering signal if they are spatially correlated or to an extremely weak background noise below the sensitivity in the performed experiments otherwise. Both contributions are neglected in the following. The remaining signal then only belongs to the ordered structure. The associated scattering signal is described by:

$$|S(\mathbf{Q})|^2 \propto |f_{mag}|^2 \left| \sum_{j=0}^{N_z-1} e^{iQ_z jc} \left(\sum_k (\epsilon^{'} \times \epsilon) \mathbf{m_0} (-1)^j m(j) e^{i\mathbf{Q}_{||}\mathbf{r}_{||}(k)} \right) \right|^2 \tag{7.20}$$

$$\propto |f_{mag}|^2 \left| (\epsilon^{'} \times \epsilon) \mathbf{m_0} \right|^2 \left| \sum_{j=0}^{N_z-1} (-1)^j m(j) e^{iQ_z jc} \right|^2 \left| \sum_k e^{i\mathbf{Q}_{||}\mathbf{r}_{||}(k)} \right|^2 \tag{7.21}$$

$$\propto |f_{mag}|^2\, P(2\Theta, \mathbf{m_0}) \left| \sum_{j=0}^{N_z-1} (-1)^j m(j) e^{iQ_z jc} \right|^2 \left| S_{2D}(\mathbf{Q}_{||}) \right|^2 \quad , \tag{7.22}$$

where $P(2\Theta)$ describes the polarization dependence and S_{2D} the two-dimensional structure factor of the (111) planes. Taking this result into the initial formula (Eq. 7.17) one obtains:

$$I_{meas}(2\Theta) \propto \Phi_0\, |f_{mag}|^2\, P \left| \sum_{j=0}^{N_z-1} (-1)^j m(j) e^{iQ_z jc} \right|^2 \int_{detector} |S_{2D}(\mathbf{Q}_{||})|^2 d\Omega \quad , \tag{7.23}$$

where the integration is performed over the two-dimensional sum only, for within the small beamline divergence and detector acceptance the Q_z dependence essentially is a constant. The last step requires the substitution of the incident photon flux by a quantity that is known from experiment. The total scattered intensity is given by the incoherent sum of all the coherent magnetic volumes of the EuTe sample. If the sample surface is larger than the beam dimension $b_v \times b_h$, the illuminated sample surface will be given by $b_v \times b_h \sin^{-1}\omega$ with ω the angle of the incidence. The total number of incident photons per second, I_0, which is a known property, is given by $b_v \times b_h \times \Phi_0$. Therefore, the final result reads:

$$I_{meas}(2\Theta) \propto \frac{I_0}{\sin\omega}\, |f_{mag}|^2\, P \left| \sum_{j=0}^{N_z-1} (-1)^j m(j) e^{iQ_z jc} \right|^2 \int_{detector} |S_{2D}(\mathbf{Q}_{||})|^2 d\Omega \quad , \tag{7.24}$$

where the measured intensity is proportional to the incident intensity I_0 as expected for a sample larger than the photon beam. While the remaining integration over the detector acceptance in the data analysis usually is performed numerically, we will state the consequence of the integration assuming a transversal intensity distribution that is completely inside the detector acceptance at all Q_z. For the non-linear relation of the scattering vector $\mathbf{Q}$ and the angular position of the detector the integrations yields a geometry dependence[10] $\int_{detector} |S_{2D}(\mathbf{Q}_{||})|^2 d\Omega \propto \sin^{-1}\Theta$. The measured integrated intensity then only depends on the perpendicular lattice sum:

$$I_{meas}(2\Theta) \propto I_0 \; P \; |f_{mag}|^2 \left| \sum_{j=0}^{N_z-1} (-1)^j m(j) e^{iQ_z jc} \right|^2 \frac{1}{\sin^2 \omega} \quad . \tag{7.25}$$

Equation 7.25 includes several geometry-dependent properties, like the scattering vector, the resonant magnetic atomic form factor and the polarization factor. These geometry dependences are important in a quantitative analysis, like the evaluation of the absolute magnetic scattering strength. They, in particular, influence the shape of reflections that cover a large range of scattering angle. Therefore, a precise quantitative analysis requires knowledge of the precise influence of these geometry dependences. In addition further corrections can become necessary that depend on the sample properties, like the temperature or the macroscopic sandwich structure. These geometry dependences as well as the corresponding normalization functions are discussed in the following. The most common corrections are the Q dependence of the atomic scattering strength, the polarization factor,[11] as well as the Debye-Waller factor.

Atomic Form Factor in Resonant Magnetic Scattering

In general, the resonant magnetic atomic form factor f_{mag} does not exclusively depend on the photon energy but is a Q-dependent property. The Q dependence originates from the possibility that the scattering contributions from different parts of one single atom exhibit a phase shift. This mechanism will become relevant if the atomic size is comparable or larger than the wave lengths of the photons, which is the case in conventional x-ray diffraction. In contrast, in resonant soft x-ray scattering, this dependence is usually neglected [110] for two reasons. The typical wave lengths in that energy range are one order of magnitude larger ($\lambda > 10$ Å) than in the hard x-ray regime ($\lambda \approx 1$ Å) and the electrons involved in the resonant scattering process are strongly localized ($3d$ and $4f$ electrons in the present case) with a spatial distribution much less than the overall atomic size. The atomic form factor of the Eu^{2+} ions for resonant magnetic scattering at the M_5 threshold is not reported in literature, but known for magnetic neutron diffraction. One cannot directly apply the latter property to resonant magnetic x-ray scattering since the two magnetic scattering mechanisms are different. While the neutrons scatter directly at the $4f$ moments, the resonant magnetic scattering process involves the even stronger localized $3d$ electrons. Therefore, it is assumed that the known magnetic form factor that applies to magnetic neutron scattering from Gd^{3+} ions is an upper limit. According to [148], the modulation of the magnetically scattered intensity, caused by the magnetic form factor, would be less than 5% over the entire range of scattering angle which enters the data analysis of the EuTe Laue

[10] In general, for a diffraction feature which is sharp along all three reciprocal space directions that integral leads to a factor $\sin^{-1} 2\Theta$. The result in the present case, differs as a consequence of the essentially constant Q_z dependence within the detector acceptance.

[11] The polarization factor depends on the microscopic and macroscopic magnetic structure and is derived in detail in chapter 7.1.3.

patterns. Since that value is an upper limit, this geometry dependence is neglected throughout this thesis.

The Debye-Waller Factor

The Debye-Waller factor, which describes the damping of the scattered intensity as a consequence of the thermal vibrations and the accompanied smeared out ionic positions usually is neglected in the soft x-ray regime for the reason of only small values of Q. According to Ref. [95], the decrease of intensity with scattering vector can be estimated from:

$$I \propto e^{-2Q^2 B} \tag{7.26}$$

with

$$\begin{aligned} B &= \frac{1}{16\pi^2}\left(\frac{11492T}{A\Theta_D^2}\phi\left(\frac{\Theta_D}{T}\right)+\frac{2873}{A\Theta_D}\right) \\ \phi(x) &= \frac{1}{x}\int_0^x \frac{h}{e^h-1}\,dh \quad , \end{aligned}$$

where T denotes the temperature, A the atomic mass number and Θ_D the Debye temperature. Applying the known value of the Debye temperature from Ref. [82] of EuTe, at $T = 10$ K, the damping of the intensity at the largest Q in the present experiments is on the order of 0.1%. Consequently, also this influence is neglected in the analysis.

The Influence of Absorption

The data from the EuTe samples are influenced by absorption effects that originate from two different mechanisms, the attenuation of the incident and scattered photons in the PbTe cap layer and the absorption inside the EuTe film itself. While the latter influence is only a small but noticeable influence on the magnetic signal due to the very small thickness of the EuTe films, the former effect causes a rather significant change of the measured angular-dependent intensity. However, the correction to the measured intensity for this photon absorption within the PbTe cap layer can be readily calculated since one knows to good accuracy (i) the attenuation coefficient of PbTe at the maximum of the Eu-M_5 resonance ($\mu_{PbTe}^{-1} = 1640$ Å) and (ii) the thickness of the cap layers as a result of the structural characterization of the samples outlined in chapter 7.1.1. Therefore, this influence can be taken into account using Eq. 3.10 by multiplying the measured intensity by:

$$C_{cap} = \frac{1}{e^{\frac{-2t_{cap}\mu_{PbTe}}{\sin\omega}}} \quad , \tag{7.27}$$

where t_{cap} denotes the cap layer thickness and ω to the angle of incidence.

This does not hold for the absorption within the EuTe films. Equation 7.25 includes this influence by means of the complex scattering vector Q. However, since the Laue patterns occur at scattering angles far away from the angle of total reflection we can rewrite:

$$I_{meas}(2\Theta) \propto I_0\, P\, |f_{mag}|^2 \left|\sum_{j=0}^{N_z-1}(-1)^j m_j e^{iQ_z jc} e^{-\frac{jc\mu_{EuTe}}{\sin\omega}}\right|^2 \frac{1}{\sin^2\omega} \quad , \tag{7.28}$$

where now Q_z only refers to the real part of the scattering vector while the absorption is described by the real exponential term. As can be seen this influence directly acts on the scattered amplitudes of the individual layers and consequently enters the interference terms of the lattice sum. Therefore, a correction of the measured intensities for this absorption effect would be only completely possible when the scattering strength of each individual layer is precisely known. This is not the case in the present experiment. However, the scattering strength of the individual layers essentially is a layer independent property at low temperatures. Therefore, the measured intensity at the maximum of magnetic reflection where all the layers scatter in phase can be corrected in very good approximation by multiplying the measured intensity by:

$$C_{abs,coh} = \frac{1}{S^2} \quad , \tag{7.29}$$

where S is the sum

$$S = \frac{1}{N_z} \left| \sum_{j=0}^{N_z-1} e^{-\frac{jc\mu_{Eu}}{\sin\omega}} \right| \quad , \tag{7.30}$$

with $\mu_{Eu} = \frac{4\pi\beta}{\lambda}$, which corresponds to 75 ML for the experimentally obtained value of $\beta = 3 \cdot 10^{-3}$. Despite this correction of the absolute value of the intensity the internal absorption causes two angular-dependent modifications of the measured Laue patterns, a slight distortion of the peak shape, in particular a smearing out of the side minima and a superimposed decrease of scattered intensity toward lower angles. For the latter intensity asymmetry a rough normalization is possible by multiplying the intensities by the inverse of the mean photon flux inside the EuTe, which reads:

$$C_{abs,mean}(\omega) = \frac{N_z}{\left(\sum_{j=0}^{N_z-1} e^{-\frac{2jc\mu_{Eu}}{\sin\omega}} \right)} \quad . \tag{7.31}$$

It should be noted that this correction only accounts for the angular-dependent overall intensity asymmetry but not for the distortion of the peak shape, in particular the angular-dependent smearing out of the Laue minima will be still present. However, all studied samples are much thinner than the attenuation length even at the maximum of absorption at resonance. Therefore, this internal absorption is completely negligible in the case of the thinner EuTe samples and represents a modification of only minor relevance even in the case of the thickest studied EuTe film.

Appendix B: Simulated Annealing

Solving a complex optimization problem is difficult, since often a unique solution does not exist or no way to find it is known. A well-known example is the traveling-salesman-problem in mathematics. Such problems are typically characterized by a large number of locally optimal solutions. Common search or optimization strategies, like least-squares-fit algorithms, are based on an iterative improvement starting from an initial state, with steps only towards a better solution of the problem, i.e. they exclusively move downhill in the parameter space that describes the problem, along the direction of maximum gradient. The search will be terminated, if no further improvement can be found. Such algorithms, applied to the above-mentioned problems, usually get stuck in a local optimum and the resulting solution often strongly depends on the initial state.

In 1983, Scott Kirkpatrick et al. introduced the concept of simulated annealing [149] as an optimization tool that can overcome these limitations by allowing to move uphill during the optimization process. This strategy exploits the analogy between statistical mechanics and combinatorial optimization. Consider the problem of perfect crystal growth from an initial metal melt: At high temperatures, the melt is characterized by a rather random arrangement of atoms at the positions r_a. Different atomic arrangements differ in potential energy $E([r_a])$, where $[r_a]$ denotes the entire set of atomic positions. The probability of the system to be in a state $[r_a]$ is given by its Boltzmann probability factor $e^{-\frac{E([r_a])}{kT}}$. As long as the temperature is well above the melting point, a large number of atomic arrangements are of nearly equal probability. Therefore, the system is in rapid change. If such a melt is cooled very rapidly, one will end up with a frozen melt, characterized by the absence of crystal order and with a potential energy well above the ground-state energy. However, the low temperature prevents the large rearrangements, necessary to reach an energetically more favorable state. On the other hand, if the melt is cooled down very slowly, the increasing differences of the Boltzmann weights of the different states with decreasing temperature force the system to realize more and more only the energetically favorable arrangements and one ends up with a perfect crystal. The simulated annealing algorithm treats optimization problems in an analogous way.

For that purpose, one has to define quantities that correspond to those describing the behavior of the metal melt: The possible states are described by a set of parameters $[m_j]$, which corresponds to the atomic positions within the melt. The problem is quantified by a so-called cost or objective function $O([m_j])$, where the solution is characterized by a minimum value of the objective function. $O([m_j])$ is the analog of the potential energy. The temperature is replaced by a control parameter, T, in the units of the objective function. Starting with an initial set of parameters, the algorithm varies these parameters by means of a random walk. In each step, the new set of parameters $[m_j]_{new}$ will be accepted, (i) if it corresponds to a smaller value of the objective function or (ii) otherwise, with a non-zero probability given by $e^{-\frac{O([m_j]new)-O([m_j]_{old})}{T}}$. This rearrangement algorithm, schematically shown in Fig. 7.35, was introduced by Metropolis et al. [150]. The non-zero probability to accept a change that leads to a larger value of the objective function, i.e. a worsening of the solution, prevents

this algorithm to get stuck in a local optimum. The additional modification in the simulated annealing method is the cooling schedule, i.e. the control parameter T is systematically reduced after a certain number of Metropolis loops. If the cooling is performed in a proper way, one will end up with the global optimum solution. This optimization tool was applied to a variety of problems such as the above-mentioned traveling salesman problem, integrated chip design, as well as in the field of physics to study spin-glass ground states [151] or to the problem of reconstruction of large and complex unit cells from x-ray and neutron diffraction data [152, 153].

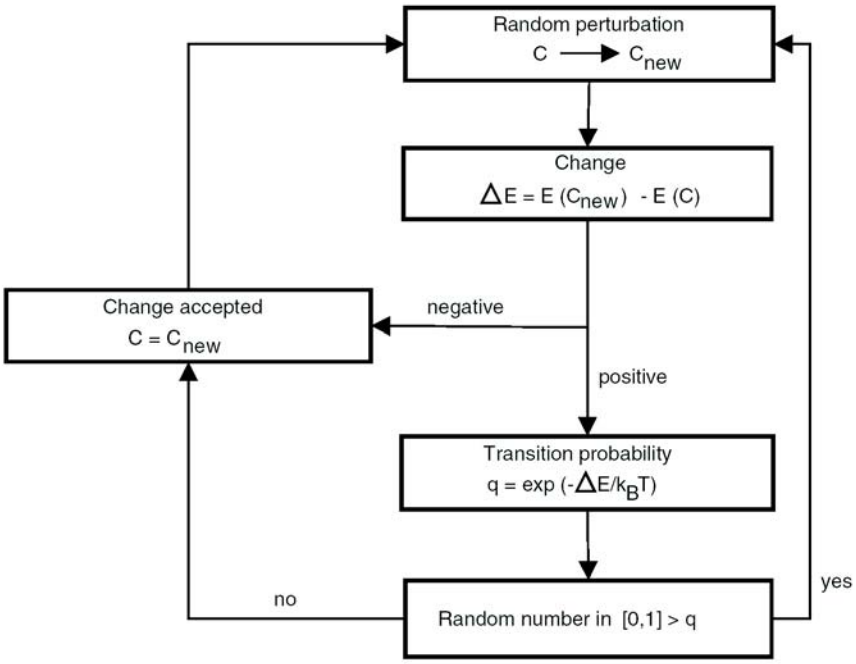

Figure 7.35: *Logical scheme of the Metropolis algorithm (from Ref. [154]).*

In the present work, an optimization algorithm was applied to the problem of the reconstruction of magnetization profiles from measured magnetic Laue patterns (chapter 7), which is based on the concepts of simulated annealing. A set of parameters was used to describe a real-space scattering-strength profile and to calculate the corresponding auto-correlation function. The difference to the experimental auto-correlation function, in terms of χ^2, was used as the objective function. The optimization of the parameters was performed by repeated Metropolis loops with a decrease of the control parameter T by 20%, after a certain number of loops. Each Metropolis loop changed one randomly chosen parameter, by a random value within a defined interval.

The analysis was carried out in two steps. In the first step, each magnetization profile was described by 22 free parameters, representing the scattering strengths of the individual layers. The optimization procedure varied 64 sets of 22 free parameters simultaneously, each set describing the scattering strength profile associated with one measured Laue pattern. In order to minimize the probability of physically meaningless solutions, the random changes of the parameters were restricted in such a way that each layer magnetization decreased monotonically with temperature, which defined the interval for each change. An upper global limit for all parameters was introduced, given by $1.2 \cdot s_0$, with a maximum scattering strength s_0 obtained from the Laue pattern measured at the lowest temperature reached in the experiment. Starting with $T = 20$, the control parameter was reduced after

10^6 Metropolis loops. The optimization stopped after five reductions of T without improvement.

In the second step, the scattering strength profile was parameterized by a function as described in chapter 7, thus avoiding unphysical jumps and oscillations of the scattering strength. The 7 parameters used to describe the scattering-strength profiles by means of this function are tabulated in table 7.4. The optimization of these parameters followed the scheme discussed above. The maximum step size in each step was restricted to 5% of the range of permitted values given in table 7.4. Starting with $T = 20$, the control parameter was reduced after 50,000 Metropolis loops found no improvement.

parameter	min. value	max. value
μ_0^{-1}	30 ML	200 ML
N_b	0	10
m_b	0	$1.2 \cdot s_0$
α	0.5	5
R	0	s_0
m_{EP}	0	1
m_{PE}	0	special

Table 7.4: *Parameters used in the second analysis step and corresponding intervals of permitted values.*

Appendix C: Refractive versus Scattering Picture

A wave that crosses the surface between vacuum and a material with an index of refraction n experiences a change of its wave vector from k in vacuum to nk in the medium. From the continuity conditions at the interface, all other aspects follow. The first obvious consequence is a phase shift of the electromagnetic wave with respect to the initial wave after passing a medium. This phase shift can be quantified by only a few atomic quantities and relates the macroscopic optical parameters δ and β to the microscopic atomic properties. This relation can be deduced by comparing the influence of an infinitesimally thin plate on a wave in the scattering and refraction pictures as depicted in Fig. 7.36: The thin plate of thickness Δ is characterized by its charge density ρ and index of refraction n. In this first step, absorption is neglected for simplicity. Let Φ_0^S denote the initial wave at S propagating along the normal direction with respect to the surface of the plate. After traversing the plate the wave at the point of observation P (Φ_{plate}^P) can be expressed in terms of the initial wave at P (Φ_0^P) in the absence of a plate $\Phi_0^P = \Phi_0^S e^{ik2R_0}$:

$$\Phi_{plate}^P = \Phi_0^P e^{i(n-1)k\Delta} \approx \Phi_0^P[1 + i(n-1)k\Delta] = \Phi_0^P[1 - ig_0] \quad , \tag{7.32}$$

with g_0 the aforementioned small phase shift.

In the scattering picture, Φ_{plate}^P results from the superposition of all the spherical waves emitted from each volume element $dxdy$ in the plate and the initial spherical wave originating from S. The initial wave at P reads $\Phi_0^P = \left(\frac{e^{ik2R_0}}{2R_0}\right)$. At the point of observation, the spherical waves $\Phi_{scattered}^P(x,y)$ emitted from a volume element at $\mathbf{R} = (x,y)$ in the plate of size $dxdy$ are given by the product of the incident wave at the plate $\left(\frac{e^{ikR_0}}{R_0}\right)$, the number of scattering centers $\rho\Delta dxdy$ and their scattering strength b. An additional phase factor $\phi(x,y)$ takes the path difference $2(R - R_0)$ into account:

$$\Phi_{scattered}^P(x,y) = \left(\frac{e^{ikR_0}}{R_0}\right)(\rho\Delta dxdy)\left(-b\frac{e^{ikR_0}}{R_0}\right)e^{i\phi(x,x)} \quad . \tag{7.33}$$

The minus sign of b realizes the phase shift of π in the scattering process and

$$\phi(x,y) = 2\left(\sqrt{R_0^2 + x^2 + y^2} - R_0\right)\frac{2\pi}{\lambda} \approx 2k\left(R_0 + \frac{x^2+y^2}{2R_0} - R_0\right) = k\frac{x^2+y^2}{R_0} \tag{7.34}$$

so that the total scattered wave at P reads:

$$\Phi_{plate}^P = \Phi_0^P + \int \Phi_{scattered}^P(x,y)dxdy = \Phi_0^P\left[1 - i\frac{2\pi\rho b\Delta}{k}\right] \quad . \tag{7.35}$$

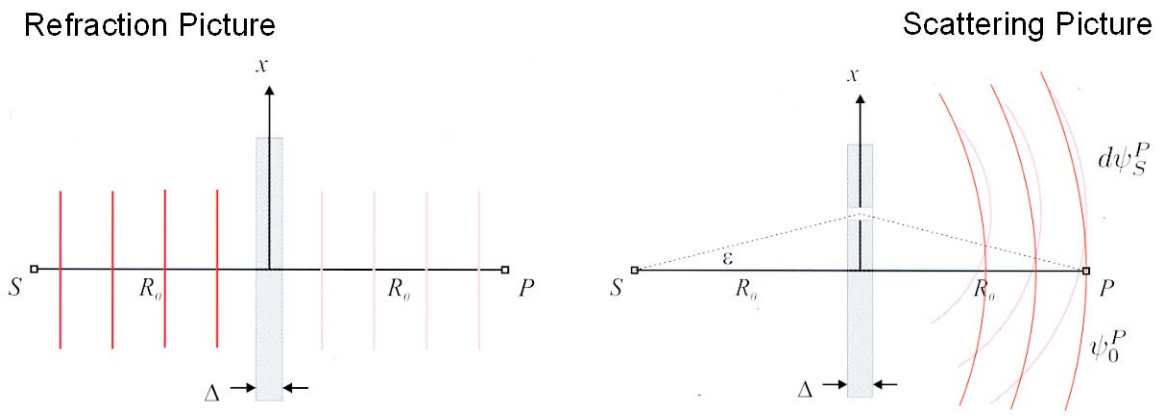

Figure 7.36: *The two equivalent pictures describing the interaction of a thin plate of thickness Δ with an electromagnetic wave. Left: Refractive picture: The wave vector changes from k to nk within the medium. n denotes the index of refraction of the plate. At the point of observation P the wave is phase-shifted compared to the initial wave. Right: Scattering picture: At P, the wave is given by the superposition of the initial wave and all the infinitesimal spherical waves radiated from the scattering centers within the plate (from Ref. [95]).*

Comparison of Eqs. 7.32 and 7.35 quantifies g_0 and the index of refraction in terms of microscopic properties. Replacing the density ρ and the scattering strength b by the atomic density ρ_a and the scattering strength of an atom $r_0 f^0(0)$ yields:

$$g_0 = \frac{2\pi\rho_a r_0 f^0(0)\Delta}{k} \tag{7.36}$$

and

$$n = 1 - \frac{2\pi\rho_a r_0 f^0(0)}{k^2} = 1 - \delta \tag{7.37}$$